AGU PUBLICATIONS

JGR

Journal of Geophysical Research: Atmospheres

RESEARCH ARTICLE
10.1002/2014JD022464

Key Points:
- Nonmigrating tides are examined without using zonal wave number decomposition
- Tropical nonmigrating tides emanate mainly from Africa and South America
- Filtering by the S-SAO wind is likely important for the tidal seasonality

Supporting Information:
- Readme
- Animation S1

Correspondence to:
T. Sakazaki,
takatoshi_sakazaki@rish.kyoto-u.ac.jp

Citation:
Sakazaki, T., K. Sato, Y. Kawatani, and S. Watanabe (2015), Three-dimensional structures of tropical nonmigrating tides in a high-vertical-resolution general circulation model, *J. Geophys. Res. Atmos.*, *120*, doi:10.1002/2014JD022464.

Received 18 AUG 2014
Accepted 6 FEB 2015
Accepted article online 11 FEB 2015

Three-dimensional structures of tropical nonmigrating tides in a high-vertical-resolution general circulation model

Takatoshi Sakazaki[1], Kaoru Sato[2], Yoshio Kawatani[3], and Shingo Watanabe[3]

[1]Research Institute for Sustainable Humanosphere, Kyoto University, Uji, Japan, [2]Department of Earth and Planetary Science, Graduate School of Science, University of Tokyo, Tokyo, Japan, [3]Japan Agency for Marine-Earth Science and Technology, Yokohama, Japan

Abstract This paper investigates nonmigrating tides from the ground to the lower mesosphere using data from a high-resolution general circulation model (KANTO GCM), as well as observational data from the Sounding of the Atmosphere using Broadband Emission Radiometry instrument on board the Thermosphere-Ionosphere-Mesosphere Energetics and Dynamics satellite and from GPS radio occultation measurements obtained with the COSMIC/FORMOSAT-3 mission. We extract nonmigrating tides using a composite as a function of universal time in physical space, without performing a zonal wave number decomposition. The KANTO GCM clearly demonstrates that tropical nonmigrating tides are regarded as gravity waves excited by diabatic heating enhanced over two major continents, specifically Africa and South America. They propagate zonally, in a direction away from their sources; that is, west and eastward propagating waves are dominant on the western and eastern sides of the continents, respectively. These characteristics are observed in two satellite data sets as well, except that the amplitudes in the KANTO GCM are larger than those in the observations. Seasonal variations of nonmigrating tides are also investigated. It is suggested that filtering owing to the stratopause semiannual oscillation, as well as diabatic heating in the troposphere, is important for the seasonal variations of nonmigrating tides in the stratosphere and the lower mesosphere.

1. Introduction

Atmospheric tides are global-scale waves with periods that are integral fractions of a solar day [*Chapman and Lindzen*, 1970]. They are driven by diurnally varying diabatic heating, such as by the absorption of solar radiation by tropospheric water and stratospheric ozone and the latent heat release associated with tropical convection. Tides propagate upward, with the amplitude reaching a maximum in the mesosphere and lower thermosphere (MLT) region. Tidal winds change the distribution of atmospheric minor constituents in the middle atmosphere [*Marsh et al.*, 2002; *Sakazaki et al.*, 2013, 2015], while the breaking of tides impacts the time-mean field in the MLT through momentum deposition [*Miyahara,* 1978; *Miyahara and Wu*, 1989; *Forbes et al.*, 2006].

If the distribution of the absorbing medium is zonally uniform, solar heating produces diurnal variations that propagate westward with the apparent motion of the Sun; these Sun-synchronous components are known as "migrating" tides. Any other components are referred to as "nonmigrating" (non-Sun-synchronous) tides; they are the focus of this study. Although migrating tides are essentially dominant, previous studies have shown that nonmigrating tides also contribute to variations in the MLT, based on data from satellite measurements [*Lieberman,* 1991; *Talaat and Lieberman*, 1999; *Oberheide et al.*, 2002, 2009; *Forbes and Wu*, 2006; *Forbes et al.*, 2006; *Zhang et al.*, 2006; *Pancheva et al.*, 2010] and numerical simulations [*Lieberman and Leovy*, 1995; *Ekanayake et al.*, 1997; *Miyahara et al.,* 1999*; Hagan and Forbes*, 2002].

Most previous studies discussed nonmigrating tides in frequency versus zonal wave number space. That is, diurnal and semidiurnal tides were decomposed into zonal wave numbers and their characteristics were subsequently discussed independently for each component. For diurnal tides, the notation "DW(E)*k*" is often used to denote a westward (eastward) propagating diurnal tide with a zonal wave number *k*, and the notation D0 is used to denote a diurnal, standing oscillation. Of the diurnal nonmigrating tides, DW2, D0, and DE3 have been reported to have the largest amplitudes in the MLT [*Forbes et al.*, 2003; *Forbes and Wu*, 2006; *Zhang et al.*, 2006]. Particularly, DE3 is responsible for variations in the "wave-4" structure of ion density [*Immel et al.*, 2006; *Hagan et al.*, 2007; *Oberheide et al.*, 2011].

The dominant wave numbers are mainly attributed to the longitudinally inhomogeneous heating that is regulated by the land-sea contrast (e.g., latent heat release). *Tokioka and Yagai* [1987] showed that if the Sun-synchronous heating with a time frequency of n (cycles per day; e.g., $n=1$ and 2 correspond to diurnal and semidiurnal tides, respectively) is amplified over continents that are characterized by a zonal wave number s, tides with zonal numbers of $k=n+s$ and $k=n-s$ are excited. This is expressed by a simple equation as

$$\begin{aligned}\cos s\lambda \cos(n\Omega t_{\mathrm{LT}}) &= \frac{1}{2}\{\cos(n\Omega t_{\mathrm{LT}}+s\lambda)+\cos(n\Omega t_{\mathrm{LT}}-s\lambda)\}\\ &= \frac{1}{2}\{\cos(n\Omega t_{\mathrm{UT}}+(n+s)\lambda)+\cos(n\Omega t_{\mathrm{UT}}+(n-s)\lambda)\},\end{aligned} \tag{1}$$

where λ is longitude (rad), $\Omega = 2\pi/24$ (h^{-1}), and t_{LT} and t_{UT} are local and universal time (LT, UT; h), respectively. The relation $t_{\mathrm{UT}} = t_{\mathrm{LT}} + \lambda/\Omega$ is used for the transformation. The authors also showed that the land-sea distribution in the tropics is roughly represented by $s=4$. Thus, equation (1) shows that for diurnal tides ($n=1$), a pair of west and eastward propagating tides with $|k|=4$ is excited on an "LT" basis, corresponding to $k=5$ (DW5) and $k=-3$ (DE3) tides, respectively, on a "UT" basis. In fact, the dominance of these wave numbers was confirmed by diurnal heating rates estimated based on rainfall data [*Williams and Avery*, 1996; *Forbes et al.*, 1997; *Zhang et al.*, 2010b]. In addition to diabatic heating, wave-wave interactions (e.g., tide-planetary wave interactions) also excite nonmigrating tides in the extratropics [*Teitelbaum and Vial*, 1991; *Hagan and Roble*, 2001; *Lieberman et al.*, 2004; *Yoshikawa and Miyahara*, 2005; *Xu et al.*, 2013].

As well as excitation processes, dissipation and filtering are important to determine the dominant wave numbers. Waves characterized by longer vertical wavelengths are less subject to dissipation. Waves with a large phase velocity (c) can propagate into the MLT without reaching their critical levels (z), where $U(z)=c$ (U is the background zonal wind velocity). For the DE3 and DW5 excited by $s=4$ (equation (1)), because of the longer vertical wavelength ($\lambda_z \sim 55$ km for the lowest Hough mode) and faster zonal phase velocity ($c_x \sim 150\ \mathrm{m\,s^{-1}}$) of DE3 compared with DW5 ($\lambda_z \sim 20$ km for the lowest Hough mode; $c_x \sim -90\ \mathrm{m\,s^{-1}}$), DE3 is expected to survive even at high altitudes and to be observed more clearly than DW5 [*Williams and Avery*, 1996; *Forbes et al.*, 2006; *Zhang et al.*, 2012]. However, note that it is not well understood at which altitudes/during which seasons the filtering processes prevail. In mechanistic models of tides, such as the global-scale wave model [*Hagan et al.*, 1995; *Zhang et al.*, 2010a, 2010b], such filtering processes are parameterized as "dissipation" processes.

As outlined above, zonal wave number decomposition helps to understand the characteristics of nonmigrating tides. We suggest, however, that the full picture of nonmigrating tides is still unclear based solely on this approach, because tides are essentially the aggregate of many zonal wave number components. Particularly, the geographical distribution of nonmigrating tides is not established. Thus, it is worth investigating nonmigrating tides as a whole in physical space, without applying zonal wave number decomposition.

Note also that only a limited number of studies have examined nonmigrating tides in the stratosphere, while there are some studies which considered migrating tides in the stratosphere [*Zeng et al.*, 2008; *Huang et al.*, 2010; *Pirscher et al.*, 2010; *Xie et al.*, 2010; *Sakazaki et al.*, 2012]. However, radiosonde soundings have confirmed the presence of nonmigrating tides in the lower stratosphere [*Wallace and Tadd*, 1974; *Alexander and Tsuda*, 2008]. Based on modeling studies, *Kawatani et al.* [2003, 2009] found that gravity waves excited by diurnal cycles of tropical deep convection over the Amazon and Africa contribute to the localized potential energy (PE) distribution in the lower stratosphere. *Horinouchi et al.* [2003], using data from several general circulation models (GCMs), found that the vertical component of the Eliassen-Palm (EP) flux (F_z) associated with nonmigrating tides (particularly, DW5 and DE3) is comparable with that for migrating tides. These studies imply the importance of nonmigrating tides in the stratosphere.

Recently, *Watanabe et al.* [2008] developed a high-resolution spectral climate model covering the region from the ground to the mesosphere. The temporal and vertical resolution of the output data is 1 h and ~300 m (in the middle atmosphere), respectively, enabling us to investigate the detailed tidal characteristics over a wide range in altitude. In addition, data from the Sounding of the Atmosphere using Broadband Emission Radiometry (SABER) instrument on board the Thermosphere-Ionosphere-Mesosphere Energetics and Dynamics (TIMED) satellite and from the Global Positioning System (GPS) radio occultation (RO) measurements, both of which measure the stratospheric temperature at different LTs, have been collected for over a decade. It should now be possible to extract statistically stable signals of nonmigrating tides from these measurements as well.

The purpose of this study is to reveal the full picture of nonmigrating tides in the tropics, from the ground to the mesosphere. By extracting and examining nonmigrating tides without performing zonal wave number decomposition, we demonstrate a new perspective of nonmigrating tides. It is also demonstrated that filtering by zonal wind is likely important for the seasonal variations of nonmigrating tides. The remainder of this paper is organized as follows. Sections 2 and 3 describe the data set and our analysis methods, respectively. Section 4 examines nonmigrating tides in physical space. Section 5 discusses the seasonal variations mainly from the viewpoint of filtering by zonal wind, while section 6 discusses the impact of nonmigrating tides on the time-mean field. Section 7 summarizes our main results.

2. Data

Output data from a Model for Interdisciplinary Research on Climate (MIROC)-based GCM developed for the KANTO project (hereafter referred to as the KANTO GCM) form the basis of the analysis performed in this study. In order to validate the characteristics of nonmigrating tides in the model, temperature data from two satellite measurements are analyzed and compared; one data set is acquired by the SABER instrument on board the TIMED satellite [*Russell et al.*, 1999], the other is based on GPS-RO measurements of the COSMIC/FORMOSAT-3 mission [*Anthes et al.*, 2008]. Details are given in the following subsections.

2.1. KANTO GCM

We use 3 year output from simulations of a high-resolution global spectral climate model [*Watanabe et al.*, 2008]. This model is based on the atmospheric component of version 3.2 of the MIROC, a coupled atmosphere-ocean GCM developed collaboratively by the Center for Climate System Research at the University of Tokyo (Japan), the National Institute for Environmental Studies (Japan), and the Frontier Research Center for Global Change (Japan) [*K-1 Model Developers*, 2004]. The model covers the vertical range from the ground up to 85 km. The horizontal resolution is T213, resulting in simulated waves with wavelengths $>$190 km. The vertical resolution is 300 m at altitudes above 10 km, which is sufficient to simulate realistic propagation and momentum deposition of the majority of observed gravity waves, including tides. No gravity wave parameterizations are included, i.e., all gravity waves (including tides) are internally generated. The time integration was done over three model years in which realistic seasonal variation was specified for the sea surface temperature (monthly mean climatology averaged between January 1979 and January 1989) and stratospheric ozone. For ozone, the zonal mean climatology is adopted, so that nonmigrating tides are not generated from the ozone layer. *Suvorova and Pogoreltsev* [2011], using numerical simulations, showed that a longitudinally inhomogeneous ozone distribution has no significant impact on the nonmigrating tides.

Previous studies showed that simulated large-scale dynamical features in the KANTO GCM are realistic [*Watanabe et al.*, 2008], including the tropopause and stratopause structures [*Tomikawa et al.*, 2008; *Miyazaki et al.*, 2010], quasi-biennial oscillation (QBO)-like oscillations [*Kawatani et al.*, 2010a], and stratopause semiannual oscillations (S-SAO) [*Watanabe et al.*, 2008]. Dominant sources and propagation of mesospheric gravity waves have also been studied from a global perspective using this data set [*Sato et al.*, 2009]. Dynamics of high-latitude middle atmosphere were also examined [*Watanabe et al.*, 2009; *Sato et al.*, 2012; *Tomikawa et al.*, 2012].

We analyze dynamical variables, as well as two heating rates (K s^{-1}), one from physical processes and the other from moist processes. The former is the total diabatic heating rate (moist processes, radiative processes, diffusion processes, and dry convective processes). The moist processes are associated with large-scale condensation and cumulus convection. In this model, the cumulus parameterization is based on that of *Arakawa and Schubert* [1974], adopting a relative humidity method (for details, see *Watanabe et al.* [2008]). Finally, the difference between the two heating rates (i.e., the heating rate from physical processes and that from moist processes) is almost equivalent to the heating rate due to radiative processes, except around the boundary layer, where diffusion and dry convective processes are dominant.

These physical quantities were sampled every hour, as hourly averages. Data are provided in terms of pressure levels, so that the results are shown based on log-pressure coordinates, where the reference pressure and scale height are set at 1000 hPa and 7 km, respectively.

2.2. SABER

The SABER instrument was launched on board the TIMED satellite on 7 December 2001. It measures the CO_2 infrared limb radiance from approximately 20 to 120 km in altitude and retrieves kinematic temperature

profiles [*Remsberg et al.*, 2008]. The latitude coverage on a given day extends from approximately 53° in one hemisphere to 83° in the other. Approximately every 60 days, the satellite performs yaw maneuvers. As a result, data are continuously obtained between 53°S and 53°N. The TIMED satellite is not in a Sun-synchronous orbit, and the LT of SABER measurements changes by about 12 min d^{-1}. Thus, the observations cover a full diurnal cycle over a period of 60 days from the ascending/descending nodes. Note that data are not acquired by SABER near local noon. The vertical resolution of the measurements is ~2 km.

In this study, version 2.0 temperature data on pressure levels are analyzed for a period of 7 years between January 2006 and December 2012. Prior to further analysis, as described in section 3, data were averaged in bins of 15° in longitude, 5° in latitude, and 2 km in log-pressure vertical coordinates, for each day and for each ascending and descending node. Here the definition of the log-pressure levels is the same as for the KANTO GCM data.

2.3. COSMIC GPS-RO

The six low-Earth-orbit (LEO) satellites of the COSMIC mission were launched in April 2006 into a circular, 72° inclination orbit at an altitude of 512 km [*Anthes et al.*, 2008]. The LEO satellites measure the phase delay of radio waves from GPS satellites as they are occulted by the Earth's atmosphere. From the phase delay, atmospheric refractivity profiles are obtained. The refractivity is then used to derive the "dry" temperature under the assumption that water vapor pressure and electron density are 0 [*Anthes et al.*, 2008].

In this study, the dry temperature data set compiled by the COSMIC Data Analysis and Archival Center is analyzed for the 5 years between 2007 and 2011. We only analyze data for altitudes between 14 and 35 km, because the effect of water vapor is nonnegligible ($>$0.1 K; i.e., the "dry" assumption is not valid) in the tropics below 14 km [e.g., *Scherllin-Pirscher et al.*, 2011]. Because the measurement locations and times are random, data during the entire 5 year period have been binned and averaged in bins of 15° in longitude, 5° in latitude, 0.5 km in geometric altitude, and 1 h in time (UT). Each hourly bin stored at least ~30 profiles in the tropics. Because of the relatively small amount of data, seasonal variations cannot be explored based on the COSMIC data.

Recently, *Khaykin et al.* [2013] investigated diurnal temperature variations in the stratosphere using COSMIC data. Note that they mainly focused on the difference in variations between land and ocean. That is, nonmigrating tides that propagate horizontally, for example, from land to ocean, were not studied in detail. Here we apply an alternative method to COSMIC data in order to extract nonmigrating tides (see section 3).

3. Analysis Methods

We note again that this study investigates nonmigrating tides, without performing zonal wave number decomposition. Monthly mean or annual mean nonmigrating tides are derived and discussed. Tides are conventionally defined as "global-scale" waves (e.g., zonal wave number $<$10 or wavelength $>$4000 km), but the nonmigrating tides extracted in this study include all waves that can have all zonal wave numbers but only have frequencies of diurnal harmonics (diurnal, semidiurnal, etc.). As the KANTO GCM provides hourly full-grid data, a simple composite analysis as a function of UT is performed at each grid point. For SABER and COSMIC, the contamination associated with their temporally and spatially inhomogeneous sampling patterns needs to be removed. Details are described in the following subsections.

3.1. KANTO GCM

Hourly output from KANTO GCM is analyzed. First, hourly diurnal variations in UT (i.e., tides including both migrating and nonmigrating components) are extracted by taking hourly UT means (e.g., average of 0000 UTC and average of 0100 UTC), followed by subtraction of their daily mean values. As an example, the longitude-altitude distribution of temperature tides at the equator at 1200 UTC is shown in Figure 1a. Next, by averaging data at the same LT for each latitude band, hourly migrating tides that are a function of LT are calculated. For example, the migrating tidal component at 0000 LT is the average of 24 data points at (0000 UT, 0°E), (0100 UT, 345°E), (0200 UT, 330°E),…, (2300 UT, 15°E). The migrating tidal component data based on LT are then converted to UT for each grid point (e.g., the data point pertaining to (0000 UT, 7.5°E) corresponding to the data at 0030 LT is calculated as the average of two data at 0000 LT and 0100 LT). Figure 1b shows the extracted migrating tides. Wave numbers 1 and 2 are dominant and correspond to diurnal and semidiurnal migrating tides, respectively. Finally, nonmigrating tides are obtained by subtracting the migrating tides

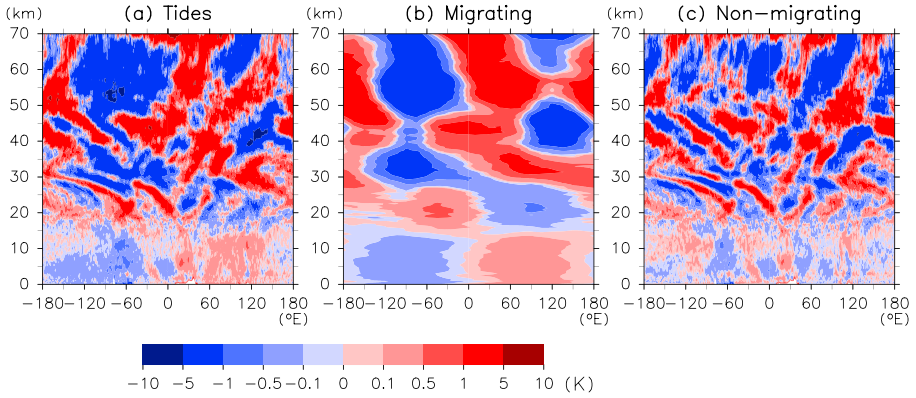

Figure 1. Longitude-altitude distributions of (a) both migrating and nonmigrating tides, (b) migrating tides, and (c) nonmigrating tides at 0°N, 1200 UTC, in January, derived from KANTO GCM data. See text for methods for extracting migrating and nonmigrating tides.

(see Figure 1b) from tides containing all components (see Figure 1a). The nonmigrating tides extracted in this way are shown in Figure 1c. Detailed structures are clearly observed in the nonmigrating tides.

Nonmigrating tides are also discussed in spectral space. In this study, diurnal components of the nonmigrating tides (i.e., $n = 1$, in units of cycles d^{-1}) are examined, because they are dominant. The method used for zonal wave number decomposition follows that of *Haurwitz and Cowley* [1973]. In the following, quantities denoted by an overbar mean daily averages, while primes indicate the extracted nonmigrating tides. The PE for the k component of each zonal wave number is calculated as

$$\mathrm{PE}_k = \frac{1}{4}\left(\frac{g}{\overline{N}}\right)^2\left(\frac{T_k}{\overline{T}}\right)^2, \tag{2}$$

where g is the acceleration due to gravity, N the Brunt-Väisalä frequency, T denotes temperature, and T_k is the amplitude of the kth component.

To examine the impact of nonmigrating tides on the time-mean zonal wind, the vertical component of the EP flux (F_z) and its divergence are calculated in section 6. In order to compare the contribution to the total flux from various wave components, we calculate the flux employing 2-D spectral analysis following *Horinouchi et al.* [2003]. The flux associated with each n and k component is expressed as [see *Horinouchi et al.*, 2003, Appendix A]

$$\begin{aligned} F_z &= \rho_0 \cos\varphi \times \left\{ \left[f - (a\cos\varphi)^{-1}(U\cos\varphi)_\varphi \right] \overline{v'\theta'}/\overline{\theta}_z - \overline{u'w'} \right\} \\ &= \rho_0 \cos\varphi \times \mathrm{Re}\left\{ \left[f - (a\cos\varphi)^{-1}(U\cos\varphi)_\varphi \right] \hat{v}(k,n)\hat{\theta}^*(k,n)/\overline{\theta}_z - \hat{u}(k,n)\hat{w}^*(k,n) \right] \right\}. \end{aligned} \tag{3}$$

Here an asterisk denotes a complex conjugate, ρ_0 is the density, ϕ the latitude, z the altitude on log-pressure coordinate, f the Coriolis parameter, a the radius of the Earth, and v and θ are the meridional wind and potential temperature, respectively. A hat denotes the Fourier coefficient of the relevant variable. Following *Horinouchi et al.* [2003], the flux due to diurnal, westward (eastward) propagating nonmigrating tides is obtained by integrating the spectral density in equation (3) over $0.97 < n < 1.03$ and $k \geq -2$ ($k \leq -1$) in the spectral domain. Note that $k = 0$ is a standing wave so that it does not have vertical flux of zonal momentum. The actual spectral analysis was performed using the original, hourly 42 day data set (e.g., for January, data obtained between 25 December and 6 February were used) after removal of the mean and any linear trends. Note that the fluxes of the diurnal tides did not change significantly, even if they were calculated using the $n = 1$ component only (i.e., adopting a line spectrum). In fact, the results are also similar to those obtained for the nonmigrating tides extracted based on the composite analysis introduced earlier in this section (not shown).

3.2. SABER

The procedure of extracting tides from SABER data basically follows the method proposed by *Forbes et al.* [2008] and also adopted by *Sakazaki et al.* [2012]. First, we prepare daily data averaged in bins of 15° in longitude, 5° in latitude, and 2 km in log-pressure height, for each ascending and descending node. In this

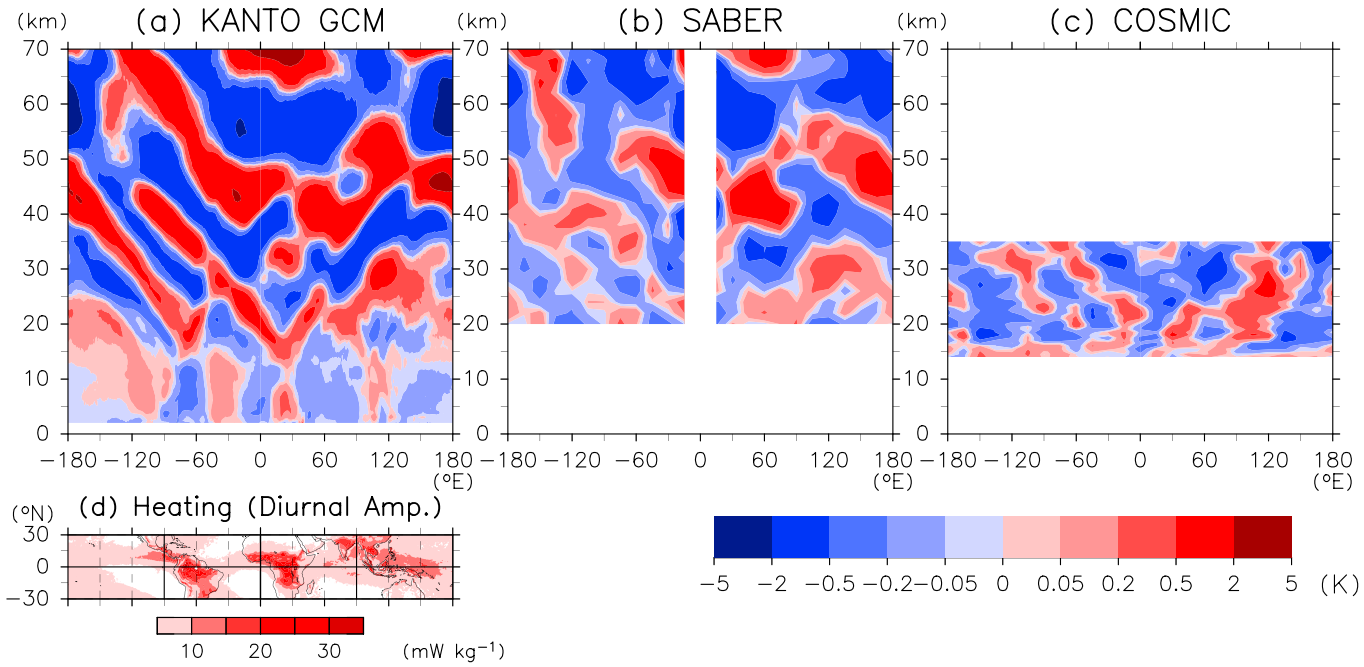

Figure 2. (a–c) Longitude-altitude distributions of multiyear mean nonmigrating temperature tides at 1200 UTC averaged over 10°S–10°N, derived from (a) the KANTO GCM, (b) SABER, and (c) COSMIC. SABER did not make measurements around local noon (around 0°E in this figure). (d) Longitude-latitude distribution of the amplitude of the diurnal harmonic component of the annual mean diabatic heating averaged between 5 and 15 km, derived from KANTO GCM output. Migrating and nonmigrating components are both included in Figure 2d.

case, each bin stores at least one data point per 1–2 days (this is because the number of orbits is 15 per day, while the number of longitude bins is 24). Next, a time series of 60 day running mean temperatures is calculated for each bin. Both ascending and descending data are used for the calculation. Because the 60 day data cover all LTs for each bin, the 60 day running mean is regarded as the daily mean, without including tidal information for any bin. Then, the 60 day running means are subtracted from the original temperatures for each day to obtain a 7 year time series of residual temperatures for each bin and for each ascending and descending node. At this stage, it is expected that a majority of slowly varying background temperature has been removed. Finally, for each month and each longitude-latitude-altitude bin, the residuals (i.e., 60 day data centered on the 15th of the month throughout the 7 years) are binned and averaged into hourly UT time bins to obtain hourly diurnal variations.

Now that hourly diurnal variations are obtained on a UT basis, the next steps are the same as those applied to the KANTO GCM data. That is, migrating tides are calculated and subtracted from the original hourly variations to obtain nonmigrating tides.

3.3. COSMIC GPS-RO

As described in section 2.3, we have prepared data in hourly UT bins for each longitude-latitude-altitude grid point. For this data set, the daily mean is calculated at each grid point by averaging data over 24 h. Then, the daily mean was subtracted from the original hourly data so that hourly diurnal variations in UT were obtained. The subsequent procedure to extract nonmigrating tides is the same as that used for KANTO GCM and SABER data (see section 3.1). Because the number of data is not sufficient to examine seasonal variation, the 5 year mean tides are obtained and discussed.

4. Nonmigrating Tides in Physical Space

This study focuses on the tropical nonmigrating temperature tides that are averaged for latitudes between 10°S and 10°N, because they have large amplitudes in this region (see Figure 8).

Figure 2 shows the longitude-altitude plot of a multiyear mean (3 years for KANTO GCM, 2006–2012 for SABER, and 2007–2011 for COSMIC) of nonmigrating tides in temperature at 12 UTC (see also Animation S1 of

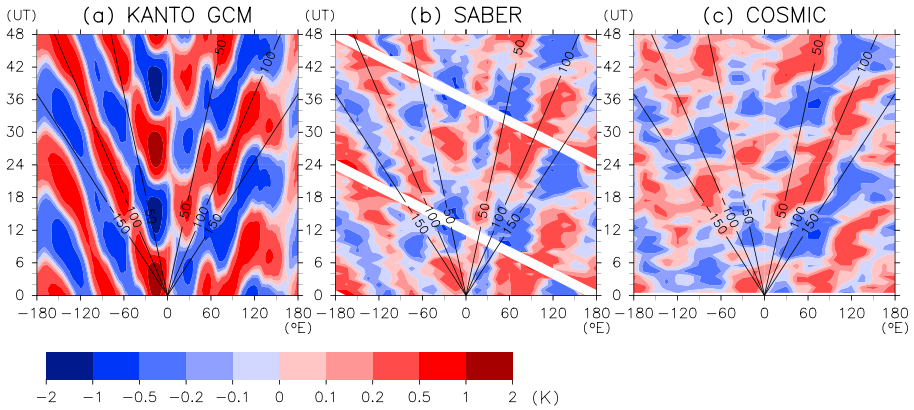

Figure 3. Hovmöller plot of the multiyear mean nonmigrating temperature tides averaged over 10°S–10°N at a height of 30 km, derived from (a) the KANTO GCM, (b) SABER, and (c) COSMIC. Black solid lines with labels show reference phase velocities (m s^{-1}). SABER did not make measurements around local noon, shown by the white areas in Figure 3b.

nonmigrating tides in January of the second year based on the KANTO GCM in the supporting information). Although the amplitudes of nonmigrating tides in the KANTO GCM are approximately 2–3 times larger than those associated with the satellite measurements, all data sets clearly demonstrate that nonmigrating tides emanate like gravity waves, mainly from two major continents, Africa (0°E–45°E) and South America (80°W–40°W), and partially from the maritime continent (100°E–150°E). On the western and eastern sides of the two major continents, the phase planes tilt westward and eastward, respectively, with increasing altitude.

Figure 2d shows the amplitude of the diurnal harmonic of the diabatic heating rate averaged over heights between 5 and 15 km from KANTO GCM data. As reported by previous studies [*Salby et al.*, 1991; *Bergman and Salby*, 1997; *Lieberman et al.,* 2007], diurnal heating is strong over the two major continents, indicating that these are dominant sources regions. The enhanced heating rate over the continents is nearly equally attributed to moist processes and radiative processes in the KANTO GCM (not shown). Relatively weaker nonmigrating tides from the Maritime Continent may be due to the incoherent heating rate (i.e., precipitation) patterns over this region, with its amplitude and phase being largely different between land (island) and ocean [*Ricciardulli and Sardeshmukh*, 2002; *Dai et al.*, 2007].

Figure 3 shows the Hovmöller plot of nonmigrating tides at a height of 30 km. Nonmigrating tides propagate their phases in a direction away from either of the two continents, which are located at ~60°W (South America) and ~30°E (Africa). This is consistent with horizontal propagation characteristics of gravity waves. Note that west and eastward propagating waves correspond to the west and eastward tilting waves in Figure 2, respectively. The phase pattern shows downward progression with time for both west and eastward propagating waves (see Animation S1), as is consistent with gravity waves propagating energy upward.

Our findings thus suggest that nonmigrating tides are regarded as internal gravity waves emanating mainly from the two "tidal fountains": the African and South American continents. As a result, westward waves are dominant in the Western Hemisphere and eastward ones are dominant in the Eastern Hemisphere, exhibiting a strong geophysical distribution. We emphasize that this perspective of nonmigrating tides has been demonstrated for the first time in this study and that it cannot be deduced from a zonal wave number decomposition.

The marked packet of westward waves in the Western Hemisphere stratosphere has a zonal wavelength (λ_x) of ~8000 km ($k \sim 5$) and a vertical wavelength (λ_z) of ~20 km (Figure 2) with its zonal phase velocity being between -80 and -100 m s^{-1} (Figure 3). In the lower mesosphere, we see larger horizontal-scale components with wave numbers of 0–3. The dominance of these waves is also confirmed in Figure 4 which shows monthly averaged PE of diurnal tides for each zonal wave number component at 50–60 km (lower mesosphere) and 25–35 km (stratosphere), as derived from KANTO GCM. The PE maxima, in fact, appear at DW5 particularly in the stratosphere. Previous studies reported a minor contribution of DW5 to nonmigrating tides in the MLT, but we

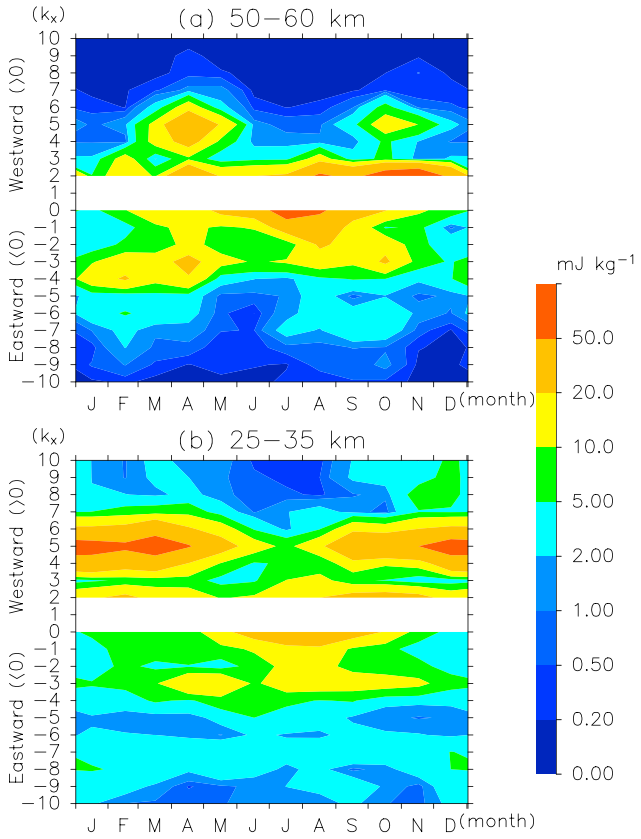

Figure 4. Month versus zonal wave number distributions of PE of diurnal tides averaged over 10°S–10°N and for altitudes (a) between 50 and 60 km and (b) between 25 and 35 km, derived from KANTO GCM data. Positive and negative zonal wave numbers denote west and eastward propagating components, respectively. Diurnal migrating tides ($k = 1$) are not shown.

found that DW5 is characterized by significant amplitude in the stratosphere. The PE also has maxima around at D0, DW2, and DE3, being consistent with previous findings in the MLT [e.g., *Forbes et al.*, 2006; *Zhang et al.*, 2006].

These dominant wave numbers are essentially explained by equation (1). The pair of DW5 and DE3 is due to the heating with $s = 4$. Note that Figure 2 suggests that $s = 4$ mainly comes from the African and South American continents. Since both continents have widths (d) of ~45° in longitude, waves with a wavelength of $2d$ (90° or $s = 4$ in wave number) are excited efficiently from each continent. In addition, the two continents are ~90° apart; this corresponds to one wavelength for $s = 4$, so that the excited waves from the two continents are nearly in phase and thus do not interfere with each other. The pair of D0 and DW2 is likely explained by the heating with $s = 1$ in equation (1). In fact, the heating rate from radiative processes at 5–15 km was strong from the Indian Ocean to the western Pacific (60°E–210°E) in the KANTO GCM (Figure 2d), because of the large amount of upper tropospheric water vapor in this region associated with the Walker circulation [*SPARC*, 2000].

We found that the qualitative characteristics of nonmigrating tides were in a fairly good agreement among the three data sets, although the amplitudes in the KANTO GCM were larger than those in satellite measurements. Based on this finding, the GCM results will be further investigated in section 5 in terms of seasonality. The overestimation of the amplitude may be due to an enhanced diurnal cycle precipitation rate in the KANTO GCM. Comparing with the precipitation rate from the Tropical Rainfall Measuring Mission (TRMM) 3B42 data [*Huffman et al.*, 2007] during 2002–2006, it is seen that the diurnal cycle of the precipitation rate in the KANTO GCM has a realistic global pattern, but the amplitude was larger than TRMM observations, particularly over central Africa (not shown).

5. Seasonal Variations

In this section, the second year output from the KANTO GCM is analyzed. Note that the results are similar to those in the first and third years (not shown). As will be shown later, nonmigrating tides are affected by the background zonal wind. Figure 5 shows the time series of the background zonal wind (monthly mean, zonal mean zonal wind) averaged over the latitude region between 10°S and 10°N, derived from KANTO GCM output. We see a clear S-SAO cycle in the altitude region between 40 and 60 km, in which the wind is easterly from December to February and from July to August, and westerly from March to May and from September to November. The first S-SAO cycle of the year involves a large-amplitude zonal wind; the easterly and westerly maxima are -50 and $30\ \mathrm{m\ s^{-1}}$, respectively, while they are respectively close to -40 and $30\ \mathrm{m\ s^{-1}}$ during the second [cf. *Watanabe et al.*, 2008]. These amplitudes are consistent with observations [*Garcia et al.*, 1997]. Note that the range of the zonal wind associated with QBO does not affect nonmigrating tides that have large horizontal scales ($|k| < 15$; section 5.3).

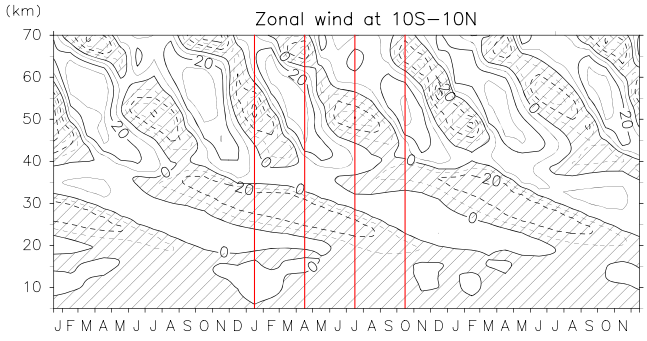

Figure 5. Month-altitude distribution of the zonal mean zonal wind derived from KANTO GCM output. Negative values (easterly winds) are hatched. Red lines denote January, April, July, and October in the second year, whose data are used to examine the seasonal variations. Contour interval is 10 m s^{-1}.

5.1. Longitude-Altitude Distribution

Figure 6 shows nonmigrating tides in temperature at 1200 UTC in January, April, July, and October from KANTO GCM data. The results were multiplied by a factor exp(−*z*/2*H*) to account for the exponential increase in amplitude, for the density scale height of $H = 7$ km. We see that the general distribution in the stratosphere does not change much with season in the sense that waves are excited and propagate from the two major continents. In contrast, we clearly see a marked seasonal variation in the mesosphere. In January and July, most westward propagating waves in the Western Hemisphere (i.e., waves whose phase is tilting westward with altitude) are abruptly dissipated around the stratopause as they approach a strong S-SAO-related easterly wind at ~50 km. As a result, only eastward propagating waves (i.e., waves whose phase is tilting eastward with

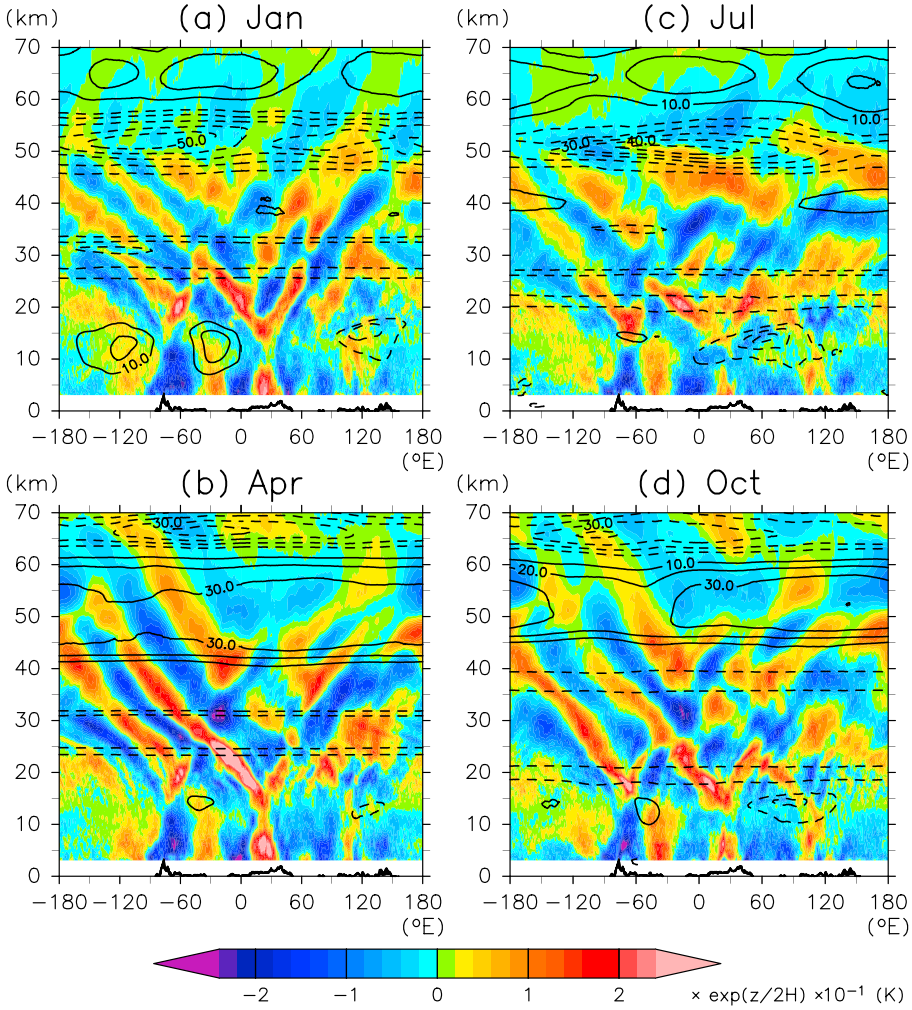

Figure 6. Same as Figure 2a but for (a) January, (b) April, (c) July, and (d) October in the second year output. The results have been multiplied by a factor exp(−*z*/2*H*), where $H = 7$ km is the scale height. Contours show monthly mean zonal wind, with solid and dashed lines indicating positive and negative values, respectively. Contour intervals are 10 m s^{-1}.

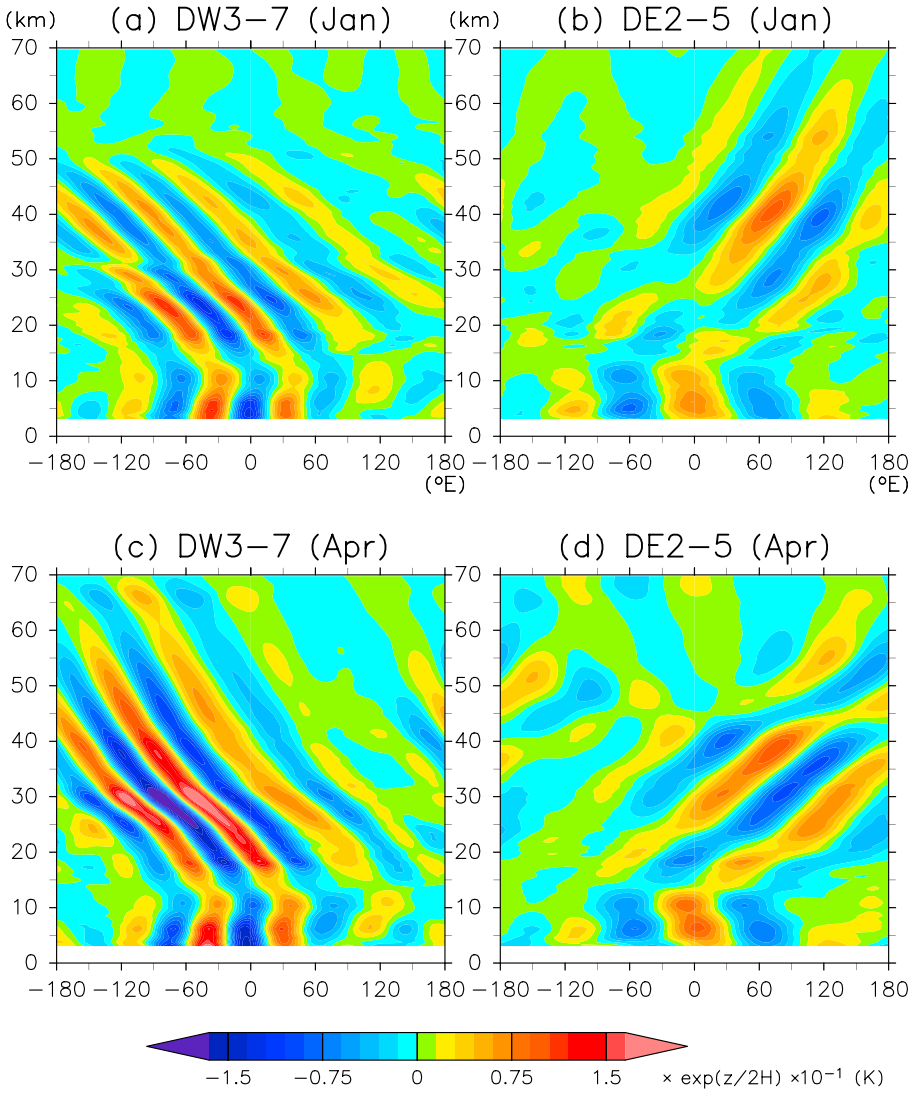

Figure 7. Same as Figure 6 but for the reconstructed diurnal tides for (a, c) westward propagating components with zonal wave numbers of 3–7 (DW5) and (b, d) eastward moving components with zonal wave numbers of 2–4 (DE3). Figures 7a and 7b are for January and Figures 7c and 7d are for April in the second year of KANTO GCM output.

altitude) survive and appear to be dominant in the mesosphere during these months. In April and October, on the other hand, the westward propagating waves penetrate deeply into the mesosphere, while eastward moving waves with $|k| = 7$–8 (e.g., waves at (0°E–150°E, 40–45 km) have wavelengths of ~50° in Figure 6b) seem to dissipate when they encounter a westerly wind at ~50 km.

These characteristics are clearer when nonmigrating tides are separated into westward and eastward components. Figure 7 shows the longitude-altitude distribution of the pair of waves generated by $s = 4$, that is, DW5 and DE3. Considering the spectral width around the peaks (see Figure 4), DW5 was reconstructed with the components between DW3 and 7, while DE3 was reconstructed with the components between DE2 and 4. As noted in the previous section, DW5 is identified as a packet of westward propagating waves appearing in the Western Hemisphere (see Figures 2 and 6). DE3 is identified as eastward propagating waves in the Eastern Hemisphere. The vertical wavelengths of DW5 and DE3 are 15–20 and 35 km, respectively.

It is clearly seen that DW5 is dissipated around the stratopause in January, while it penetrates deeply into the mesosphere in April. DE3 components, on the other hand, penetrate into the mesosphere both in January and April, although in April, DE3 is partly dissipated or deformed around the stratopause. The distribution in July (October) is similar to that in January (April; not shown), although DE3 is weak in July. This is likely due to

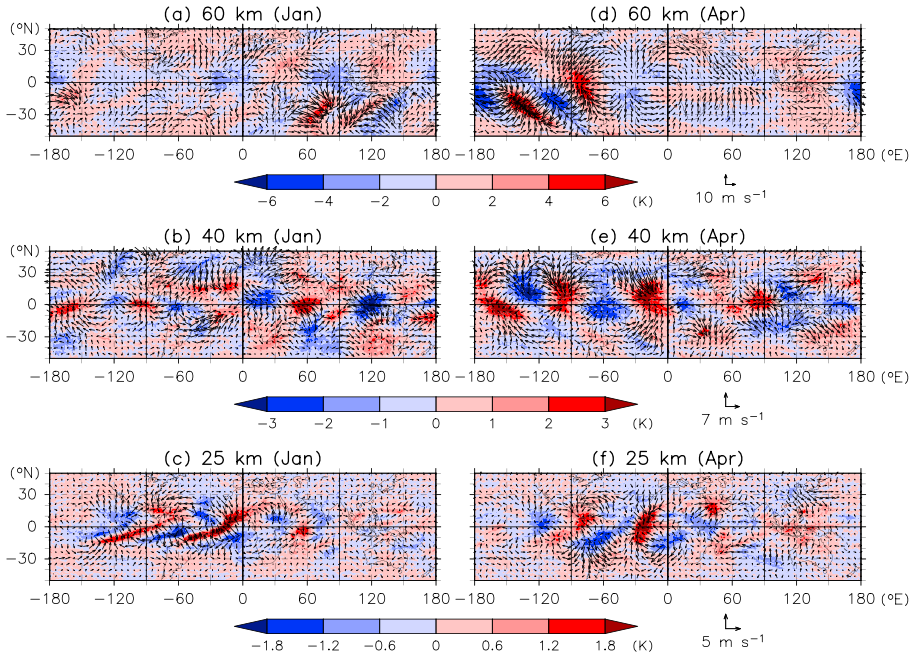

Figure 8. Longitude-latitude distributions of nonmigrating tides in (color) temperature and (vectors) horizontal winds, in January and April in the second year, derived from KANTO GCM data, for an altitude of (a and d) 60 km, (b and e) 40 km, and (c and f) 25 km.

the fact that the corresponding component of diabatic heating rate is small in this season as shown in Figure 10 in later section.

These results suggest that the seasonal changes in background zonal wind associated with the S-SAO around the stratopause strongly affect the vertical distribution of nonmigrating tides, likely through critical-level filtering processes. As far as we are aware, the importance of filtering owing to S-SAO for nonmigrating tides has thus far not been pointed out.

5.2. Latitudinal Distribution

So far, we have considered nonmigrating tides averaged over 10°S–10°N, since tides become maximal in the tropics. Here we briefly examine the latitudinal structure. Figure 8 shows the longitude-latitude distribution of nonmigrating tides in temperature and horizontal winds at 1200 UTC. High (low)-temperature anomalies correspond to the convergence (divergence) zone of horizontal winds; this relation accords with a characteristic of gravity waves. The variations are largest in the region between 30°S and 30°N as is consistent with the characteristics of diurnal tide (or gravity waves) which cannot propagate vertically outside of 30° when $U = 0$. In this latitude range, the latitudinal extent broadens with increasing altitude. At the same time, components that are antisymmetric with respect to the equator are observed, particularly in January at 25 km. This is possibly related to the seasonal migration of convective activity across the equator.

As already pointed out, we also see a geographical dependence of nonmigrating tides and its seasonality. At 25 km, a packet of waves with $|k| \sim 5$ is clearly detectable over the source regions (Africa and South America), while at 40 km the waves appear west or eastward of the source regions as well, as they propagate horizontally. In January, the waves almost disappear at 60 km because of S-SAO filtering below this level (at ~50 km). In April, the waves in the Western Hemisphere are observed even at 60 km.

5.3. Relative Importance of Filtering Effect and Diabatic Heating

In this section, first, the dependence of filtering effects on the zonal wave number is quantitatively examined. Figure 9 shows the vertical distributions of PE as a function of zonal wave number with its corresponding phase velocity. Solid curves in each panel denote the monthly mean zonal wind averaged across 10°S–10°N. The background zonal wind changes in longitude, latitude, and time should affect the local propagation of waves. Thus, the two dashed curves show the averaged zonal winds plus/minus 1.65 times their standard deviations

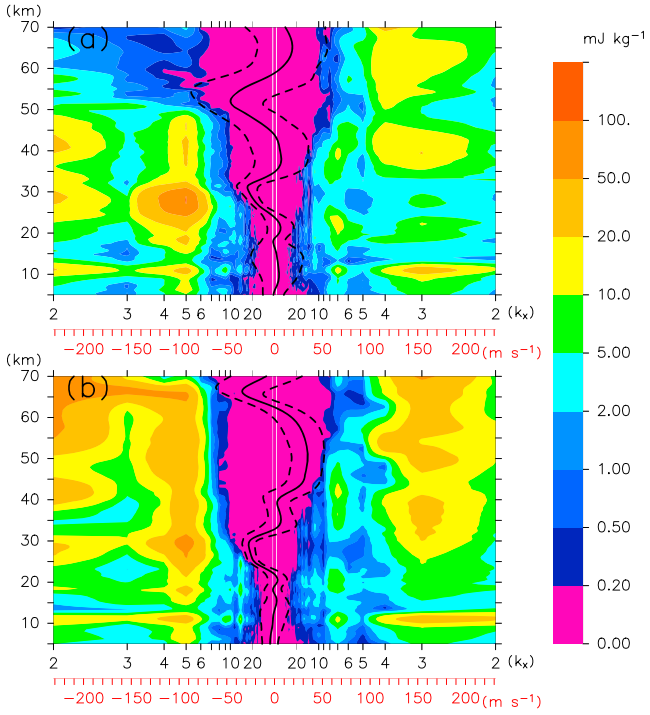

Figure 9. Zonal wave number versus altitude plot of PE in (a) January and (b) April. The corresponding phase velocity is also shown by the red *x* axes. Solid curves denote the monthly mean, zonal mean zonal wind, averaged over 10°S–10°N; dashed curves denote the average zonal winds ±1.65 times the standard deviation.

(assuming the normal distribution applies, this will include 90% of the data). The average and standard deviation are calculated using daily mean data so that tides are not included in the standard deviation.

It is found that in the lower stratosphere, nonmigrating tides with $|k| > 15$ are dissipated largely in the QBO region (see Figure 5), as is consistent with the critical-level filtering. The remaining components propagate into the upper stratosphere. In January, the S-SAO has an easterly wind of $-50 \pm 35\ \mathrm{m\,s^{-1}}$; its minimum nearly corresponds to the phase velocity of DW5 ($-90\ \mathrm{m\,s^{-1}}$), indicating that critical-level filtering could occur for $k \geq 5$. In April, on the other hand, the S-SAO produces a westerly wind of $35 \pm 20\ \mathrm{m\,s^{-1}}$; its maximum corresponds to the phase velocity of DE8, indicating that critical-level filtering could occur only for $k \leq \sim -8$.

Second, the effect of the seasonal variation of diabatic heating rate is also examined. Figure 10 shows the seasonal variation in diurnal amplitude of tropospheric diabatic heating rate averaged over 5–15 km in altitude and 20°S–20°N in latitude as a function of zonal wave number component. As dominant convections as a source of nonmigrating tides slightly move latitudinally depending on the season, we examined the heating rate averaged over the latitudes of 20°S–20°N although the structure of the tides was mainly examined for an average over 10°S–10°N. As already noted, the peaks at DE3 and DW5 are associated with the heating with $s = 4$, while those at D0 and DW2 are associated with the heating rate with $s = 1$. Both the heating rate from moist processes (Figure 10b) and that from radiative processes (Figure 10c) contribute to the total heating rate. However, it is worth noting that the two heating rates show different seasonal variations. The seasonal variation of heating rate by moist processes maximizes around at equinoxes, which is basically due to seasonal migration of Sun across the equator. The heating rate by radiative processes, in contrast, maximizes around at solstices. The peak of $s = 1$ (i.e., D0 and DW2) in Northern Hemisphere summer is possibly due to the water vapor mixing ratio in the western Pacific that increases in summer owing to the Southeast Asian/Indian monsoon [*SPARC,* 2000].

From the comparison between Figures 4 and 10, the controlling processes of the seasonal variation in nonmigrating tides can be inferred. The seasonal variation of PE in the lower stratosphere (Figure 4b) essentially follows that of diabatic heating rate in the troposphere (Figure 10). Above the stratopause (Figure 4a), the PE of DW5 becomes small in January, as is consistent with the filtering at ~50 km. In contrast, the PE of D0, DW2, and DE3 is still similar to that in the lower stratosphere. These results indicate that excitation and propagation, particularly S-SAO filtering, are both important for the seasonality of nonmigrating tides.

Previous studies of the MLT reported the "wave-4" structure for several dynamical variables at a particular "local time," which was mainly attributed to DE3 [e.g., *Forbes et al.*, 2006]. Our findings clearly demonstrate that DE3 and DW5 are excited simultaneously in the troposphere (Figure 7); however, DW5 is largely dissipated before reaching the MLT region likely because of critical-level filtering in the S-SAO region, while DE3 is not at any season during the year.

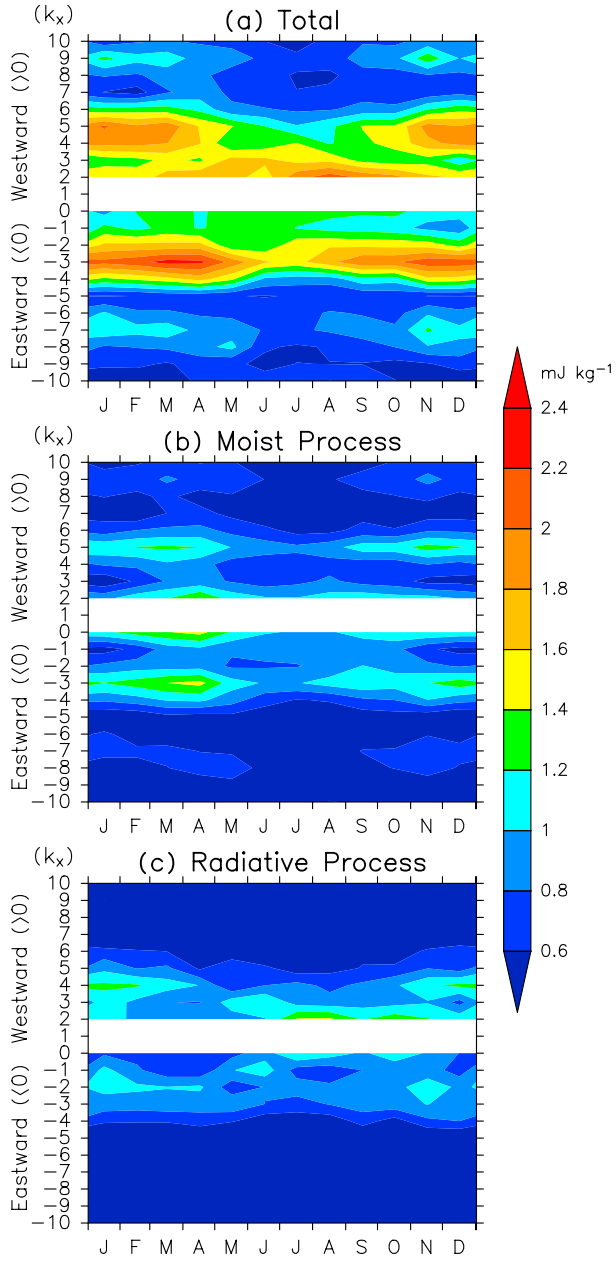

Figure 10. Same as Figure 4 but for the amplitude of the diabatic heating rate averaged over altitudes between 5 and 15 km and for latitudes between 20°S and 20°N: (a) heating rate caused by physical processes (total heating rate), (b) heating rate owing to moist processes, and (c) Figure 10a minus Figure 10b, which is regarded as the heating rate owing to radiative processes. For Figure 10c, the difference between Figures 10a and 10b is taken for 1-hourly tides; then each zonal wave number component of the diurnal tides is extracted.

6. Discussion: Tidal Impacts on Time-Mean Zonal Wind

As shown above, a part of the nonmigrating tides (e.g., DW5) is dissipated by strong zonal winds, particularly by the S-SAO wind around the stratopause. In turn, this suggests that nonmigrating tides may modify the zonal wind through momentum deposition. Thus, it is worth discussing momentum transport by nonmigrating tides in the KANTO GCM although the amplitude of nonmigrating tides in the model is larger than that in SABER and COSMIC data, because the model reproduces realistic dynamical features without using gravity wave parameterization.

We examine KANTO GCM data for the second year in January and April. In January (April), the westerly (easterly) wind descends from the lower mesosphere to the upper stratosphere. Also in this year, the QBO zonal wind is easterly at 30 km (see Figure 5). To compare various types of waves, the EP flux is calculated in the 2-D spectral domain by the method described in section 3.1. Note that in the tropics where f is small, the second term (i.e., $\overline{u'w'}$ of F_z in equation (3)) is dominant.

Figure 11 shows the vertical profile of F_z associated with various waves. It is clear that F_z by nonmigrating tides (red solid curves) is larger than that by the diurnal migrating tide (blue curves). For both west and eastward propagating waves, the ratio of the F_z associated with nonmigrating tides to the total (black solid curves) is 10–40% in the middle atmosphere. For F_z associated with westward propagating, nonmigrating tides, DW5 is a main contributor (Figures 11a and 11d, red dashed curves). For F_z by eastward moving, nonmigrating tides, DE3 is a main contributor (Figures 11b and 11e, red dashed curves).

The EP flux F_z abruptly decreases with altitude in the QBO and the S-SAO regions. The divergence of F_z and the tendency of the zonal mean zonal wind (i.e., dU/dt; green curves) are shown in Figures 11c and 11f. For the QBO, the divergence of total flux (black curves) shows negative peaks at 25–30 km both in January (see Figures 11a and 11c) and April (see Figures 11d and 11f), corresponding to the westward acceleration of −0.1 to −0.2 m s^{-1} d^{-1}. The contribution of nonmigrating tides to the total divergence (Figures 11c and 11f, red curves) is negligible compared with those from other waves (for details, see *Kawatani et al.* [2010a, 2010b]).

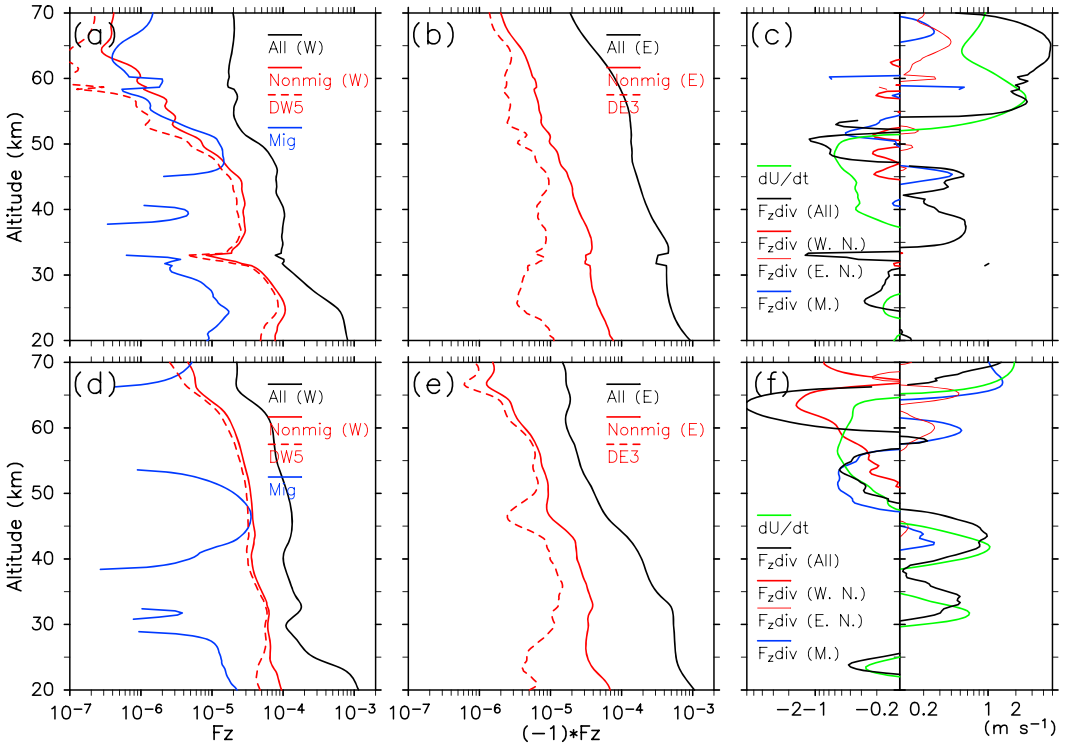

Figure 11. (a, d) Vertical component of the EP flux (F_z) associated with westward propagating waves: all westward moving waves ($k \geq 1$; black curves); westward propagating diurnal nonmigrating tides ($0.97 \leq n \leq 1.03$, $k \geq 2$; red solid curves);DW5 ($0.97 < n < 1.03$, $3 \leq k \leq 7$; red dashed curves);and diurnal migrating tides ($0.97 \leq n \leq 1.03$, $k = 1$; blue solid curves). Only negative values are plotted. (b, e) EP flux associated with eastward propagating waves: all eastward moving waves ($k \leq -1$; black curves);eastward propagating diurnal nonmigrating tides ($0.97 \leq n \leq 1.03$, $k \leq -1$; red solid curves); and DE3 ($0.97 \leq n \leq 1.03$, $-4 \leq k \leq -2$; red dashed curves). Only positive values are plotted. (c, f) Tendency of background zonal wind (green curves) and divergence of EP flux due to all waves (black curves), westward propagating diurnal nonmigrating tides (thick red curves), eastward propagating diurnal nonmigrating tides (thin red curves), and diurnal migrating tides (blue curves). Only values larger (less) than 0.1 (-0.1) are plotted for January and for April, from the second year output of the KANTO GCM.

Next, for the S-SAO, we discuss the westward and eastward accelerations, separately. For the westward acceleration phase, a negative EP flux divergence is seen at around 45–50 km in January, where dU/dt is $-1\,\mathrm{m\,s^{-1}\,d^{-1}}$. For the eastward acceleration phase, positive EP flux divergence is seen at 55 km in January and 45 km in April, where dU/dt is respectively 3 and $1\,\mathrm{m\,s^{-1}\,d^{-1}}$. The contribution of nonmigrating tides to the total EP flux divergence is negligible for the eastward acceleration phase, while it is up to 10–20% for the westward acceleration phase (at 45–50 km in January). Thus, forcing by nonmigrating tides may not be important for either of easterly and westerly phase of the S-SAO. Note that the westward S-SAO wind is thought to be driven mainly by the penetration of the summer mesospheric easterlies into the winter hemisphere [e.g., *Hirota*, 1980; *Sassi and Garcia*, 1997].

In Figure 11, the EP flux convergence and divergence are largest around at 65 km in altitude. Here it is worth noting that *Watanabe et al.* [2008] reported that the zonal wind at this level has an intraseasonal oscillation with periods of 30–60 days; the oscillation observed around 65 km in Figure 5 may be an apparent SAO-like oscillation in the "monthly" data. The negative peak around 65 km in April observed in the total EP flux divergence corresponds to an eastward acceleration of $-6\,\mathrm{m\,s^{-1}\,d^{-1}}$. The contribution of westward propagating nonmigrating tides to this peak reaches ~30%. This result supports the modeling study of *Sassi and Garcia* [1997], who showed that diurnal forcing is necessary for the easterly wind of the mesospheric SAO (M-SAO), although the M-SAO is not clear in the KANTO GCM.

In summary, while nonmigrating tides are clearly dissipated owing to the S-SAO wind, their contribution to the S-SAO is minor. However, they may be rather important for zonal wind acceleration in the mesosphere.

7. Summary

Nonmigrating tides were studied from the ground to the lower mesosphere using output data from a high-resolution GCM. We extracted and investigated nonmigrating tides as a whole, without performing zonal wave number decomposition. It is clearly demonstrated that tropical nonmigrating tides are regarded as gravity waves excited by diurnal variation in diabatic heating rate enhanced over two major continents, i.e., Africa and South America. These nonmigrating tides propagate west and eastward, in a direction away from the sources. As a result, west and eastward propagating waves are dominant on the western and eastern sides of the continents, respectively. On the western (eastern) side, a packet of westward propagating (eastward propagating) waves with a zonal wave number of 5 (3) is clearly visible. Such a marked geographical distribution has been highlighted for the first time in this study. The same characteristics were also observed in two independent satellite data sets, SABER and COSMIC.

The seasonal variations in nonmigrating tides were also investigated. The seasonal variation in both tropospheric diabatic heating and critical-level filtering caused by the S-SAO zonal wind is likely important for the seasonality of nonmigrating tides. In January and July, when the S-SAO zonal wind is easterly, westward propagating waves with $k \geq 5$ (including DW5) are dissipated around the stratopause. As a result, eastward moving waves are dominant in the mesosphere during these months. In April and October, when the S-SAO zonal wind is westerly, eastward propagating waves with $k \leq -8$ are dissipated around the stratopause. As a result, DW5 and large-scale eastward propagating waves are observed in the mesosphere. DE3, which has a phase velocity of ~150 m s^{-1}, is not dissipated by S-SAO filtering at any time during the year. The present study first identified the specific mechanism for the dissipation of DW5 and suggests that critical-level filtering by S-SAO needs to be taken into account in mechanistic tidal models.

We also discussed the impacts of nonmigrating tides on the time-mean field through zonal momentum deposition associated with the nonmigrating tidal dissipation in the S-SAO region. It was shown that the impact on the S-SAO is minor compared with that of other tropical waves. The acceleration by nonmigrating tides may be rather important in the mesosphere.

Acknowledgments

The KANTO GCM simulation was conducted using the Earth Simulator. Part of the simulation was performed as a contribution to the Innovative Program of Climate Change Projection for the 21st Century supported by the Ministry of Education, Culture, Sports, Science and Technology (MEXT), Japan. We thank the SABER science team (Jim Russell) for providing the data used in this study (obtained by FTP from ftp://saber.gatsinc.com/custom/Temp_O3/). COSMIC data were obtained from the COSMIC Data Analysis and Archive Center (CDAAC). T. Sakazaki thanks Masashi Kohma for dealing with the KANTO GCM data, Eriko Nishimoto for downloading and processing original COSMIC data, and Takenari Kinoshita, Masato Shiotani, and Toshitaka Tsuda for fruitful discussions. We are also grateful to three anonymous reviewers and the Associate Editor for their helpful comments which helped us to improve the manuscript. T. Sakazaki was supported in part by MEXT through a Grant-in-Aid for JSPS Fellows (grant 25483400). This study was supported in part by MEXT through a Grant-in-Aid for Scientific Research (A) (grant 25247075). All figures were drawn with the GFD-Dennou Library.

References

Alexander, S. P., and T. Tsuda (2008), Observations of the diurnal tide during seven intensive radiosonde campaigns in Australia and Indonesia, *J. Geophys. Res.*, *113*, D04109, doi:10.1029/2007JD008717.

Anthes, R. A., et al. (2008), The COSMIC/FORMOSAT-3 Mission: Early results, *Bull. Am. Meteorol. Soc.*, *89*, 313–333, doi:10.1175/BAMS-89-3-313.

Arakawa, A., and W. H. Schubert (1974), Interactions of cumulus cloud ensemble with the large-scale environment. Part I, *J. Atmos. Sci.*, *31*, 674–701.

Bergman, J. W., and M. L. Salby (1997), The role of cloud diurnal variations in the time-mean energy budget, *J. Clim.*, *10*, 1114–1124.

Chapman, S., and R. S. Lindzen (1970), *Atmospheric Tides*, 200 pp., D. Reidel, New York.

Dai, A., X. Lin, and K.-L. Hsu (2007), The frequency, intensity, and diurnal cycle of precipitation in surface and satellite observations over low- and mid-latitudes, *Clim. Dyn.*, *29*, 727–744, doi:10.1007/s00382-007-0260-y.

Ekanayake, E. M. P., T. Aso, and S. Miyahara (1997), Background wind effect on propagation of nonmigrating diurnal tides in the middle atmosphere, *J. Atmos. Terr. Phys.*, *59*, 401–429.

Forbes, J. M., and D. Wu (2006), Solar tides as revealed by measurements of mesosphere temperature by the MLS experiment on UARS, *J. Atmos. Sci.*, *63*, 1776–1797.

Forbes, J. M., M. E. Hagan, X. Zhang, and K. Hamilton (1997), Upper atmosphere tidal oscillations due to latent heat release in the tropical troposphere, *Ann. Geophys.*, *15*, 1165–1175.

Forbes, J. M., X. Zhang, E. R. Talaat, and W. Ward (2003), Nonmigrating diurnal tides in the thermosphere, *J. Geophys. Res.*, *108*(A1), 1033, doi:10.1029/2002JA009262.

Forbes, J. M., J. Russell, S. Miyahara, X. Zhang, S. Palo, M. Mlynczak, C. J. Mertens, and M. E. Hagan (2006), Troposphere-thermosphere tidal coupling as measured by the SABER instrument on TIMED during July-September 2002, *J. Geophys. Res.*, *111*, A10S06, doi:10.1029/2005JA011492.

Forbes, J. M., X. Zhang, S. Palo, J. Russell, C. J. Mertens, and M. Mlynczak (2008), Tidal variability in the ionospheric dynamo region, *J. Geophys. Res.*, *113*, A02310, doi:10.1029/2007JA012737.

Garcia, R. R., T. J. Dunkerton, R. S. Lieberman, and R. A. Vincent (1997), Climatology of the semiannual oscillation of the tropical middle atmosphere, *J. Geophys. Res.*, *102*(D22), 26,019–26,032, doi:10.1029/97JD00207.

Hagan, M. E., and J. M. Forbes (2002), Migrating and nonmigrating diurnal tides in the middle and upper atmosphere excited by tropospheric latent heat release, *J. Geophys. Res.*, *107*(D24), 4754, doi:10.1029/2001JD001236.

Hagan, M. E., and R. G. Roble (2001), Modeling diurnal tidal variability with the National Center for Atmospheric Research thermosphere-ionosphere-mesosphere-electrodynamics general circulation model, *J. Geophys. Res.*, *106*(A11), 24,869–24,882, doi:10.1029/2001JA000057.

Hagan, M. E., J. M. Forbes, and F. Vial (1995), On modeling migrating solar tides, *Geophys. Res. Lett.*, *22*, 893–896, doi:10.1029/95GL00783.

Hagan, M. E., A. Maute, R. G. Roble, A. D. Richmond, T. J. Immel, and S. L. England (2007), Connections between deep tropical clouds and the Earth's ionosphere, *Geophys. Res. Lett.*, *34*, L20109, doi:10.1029/2007GL030142.

Haurwitz, B., and A. D. Cowley (1973), The diurnal and semidiurnal barometric oscillations, global distribution and annual variation, *Pure Appl. Geophys.*, *102*, 193–222.

Hirota, I. (1980), Observational evidence of the semiannual oscillation in the tropical middle atmosphere—A review, *Pure Appl. Geophys.*, *118*, 217–238.

Horinouchi, T., et al. (2003), Tropical cumulus convection and upward-propagating waves in middle-atmospheric GCMs, *J. Atmos. Sci.*, *60*, 2765–2782.
Huang, F. T., R. D. McPeters, P. K. Bhartia, H. G. Mayr, S. M. Frith, J. M. Russell III, and M. G. Mlynczak (2010), Temperature diurnal variations (migrating tides) in the stratosphere and lower mesosphere based on measurements from SABER on TIMED, *J. Geophys. Res.*, *115*, D16121, doi:10.1029/2009JD013698.
Huffman, G. J., R. F. Adler, D. T. Bolvin, G. Gu, E. J. Nelkin, K. P. Bowman, Y. Hong, E. F. Stocker, and D. B. Wolff (2007), The TRMM Multisatellite Precipitation Analysis (TMPA): Quasi-global, multiyear, combined-sensor precipitation estimates at fine scales, *J. Hydrometeorol.*, *8*, 38–55.
Immel, T. J., E. Sagawa, S. L. England, S. B. Henderson, M. E. Hagan, S. B. Mende, H. U. Frey, C. M. Swenson, and L. J. Paxton (2006), Control of equatorial ionospheric morphology by atmospheric tides, *Geophys. Res. Lett.*, *33*, L15108, doi:10.1029/2006GL026161.
K-1 Model Developers (2004), K-1 coupled GCM (MIROC) description, *K-1 Tech. Rep. 1*, 34 pp., Univ. of Tokyo.
Kawatani Y., S. K. Dhaka, M. Takahashi, and T. Tsuda (2003), Large potential energy of gravity waves over a smooth surface with little convection: Simulation and observation, *Geophys. Res. Lett.*, *30*(8), 1438, doi:10.1029/2003GL016960.
Kawatani, Y., M. Takahashi, K. Sato, S. P. Alexander, and T. Tsuda (2009), Global distribution of atmospheric waves in the equatorial upper troposphere and lower stratosphere: AGCM simulation of sources and propagation, *J. Geophys. Res.*, *114*, D01102, doi:10.1029/2008JD010374.
Kawatani, Y., K. Sato, T. J. Dunkerton, S. Watanabe, S. Miyahara, and M. Takahashi (2010a), The roles of equatorial trapped waves and internal inertia-gravity waves in driving the quasi-biennial oscillation. Part I: Zonal mean wave forcing, *J. Atmos. Sci.*, *67*, 963–980.
Kawatani, Y., K. Sato, T. J. Dunkerton, S. Watanabe, S. Miyahara, and M. Takahashi (2010b), The roles of equatorial trapped waves and internal inertia-gravity waves in driving the quasi-biennial oscillation. Part I: Three-dimensional distribution of wave forcing, *J. Atmos. Sci.*, *67*, 981–997.
Khaykin, S. M., J.-P. Pommereau, and A. Hauchecorne (2013), Impact of land convection on temperature diurnal variation in the tropical lower stratosphere inferred from COSMIC GPS radio occultations, *Atmos. Chem. Phys.*, *13*, 6391–6402, doi:10.5194/acp-13-6391-2013.
Lieberman, R. S. (1991), Nonmigrating diurnal tides in the equatorial middle atmosphere, *J. Atmos. Sci.*, *48*, 1112–1123.
Lieberman, R. S., and C. B. Leovy (1995), A numerical model of nonmigrating diurnal tides between the surface and 65 km, *J. Atmos. Sci.*, *52*, 389–409.
Lieberman, R. S., J. Oberheide, M. E. Hagan, E. E. Remsberg, and L. L. Gordley (2004), Variability of diurnal tides and planetary waves during November 1978-May 1979, *J. Atmos. Terr. Phys.*, *66*, 517–528.
Lieberman, R. S., D. M. Riggin, D. A. Ortland, S. W. Nesbitt, and R. A. Vincent (2007), Variability of mesospheric diurnal tides and tropospheric diurnal heating during 1997-1998, *J. Geophys. Res.*, *112*, D20110, doi:10.1029/2007JD008578.
Marsh, D. R., W. R. Skinner, A. R. Marshall, P. B. Hays, D. A. Ortland, and J.-H. Yee (2002), High resolution Doppler imager observations of ozone in the mesosphere and lower thermosphere, *J. Geophys. Res.*, *107*(D19), 4390, doi:10.1029/2001JD001505.
Miyahara, S. (1978), Zonal mean winds induced by vertically propagating atmospheric tidal waves in the lower thermosphere, *J. Meteorol. Soc. Jpn.*, *56*, 86–97.
Miyahara, S., and D.-H. Wu (1989), Effects of solar tides on the zonal mean circulation in the lower thermosphere: Solstice condition, *J. Atmos. Terr. Phys.*, *51*, 635–647.
Miyahara, S., Y. Miyoshi, and K. Yamashita (1999), Variations of migrating and non-migrating tides simulated by the middle atmosphere circulation model at Kyushu University, *Adv. Space Res.*, *24*, 1549–1558.
Miyazaki, K., S. Watanabe, Y. Kawatani, Y. Tomikawa, M. Takahashi, and K. Sato (2010), Transport and mixing in the extratropical tropopause region in a high-vertical-resolution GCM. Part I: Potential vorticity and heat budget analysis, *J. Atmos. Sci.*, *67*, 1293–1314.
Oberheide, J., M. E. Hagan, R. G. Roble, and D. Offermann (2002), Sources of nonmigrating tides in the tropical middle atmosphere, *J. Geophys. Res.*, *107*(D21), 4567, doi:10.1029/2002JD002220.
Oberheide, J., J. M. Forbes, K. Häusler, Q. Wu, and S. L. Bruinsma (2009), Tropospheric tides from 80 to 400 km: Propagation, interannual variability, and solar cycle effects, *J. Geophys. Res.*, *114*, D00I05, doi:10.1029/2009JD012388.
Oberheide, J., J. M. Forbes, X. Zhang, and S. L. Bruinsma (2011), Wave-driven variability in the ionosphere-thermosphere-mesosphere system from TIMED observations: What contributes to the "wave 4"?, *J. Geophys. Res.*, *116*, A01306, doi:10.1029/2010JA015911.
Pancheva, D., P. Mukhtarov, and B. Andonov (2010), Global structure, seasonal and interannual variability of the eastward propagating tides seen in the SABER/TIMED temperatures (2002-2007), *Adv. Space Res.*, *46*, 257–274.
Pirscher, B., U. Foelsche, M. Borsche, G. Kirchengast, and Y.-H. Kuo (2010), Analysis of migrating diurnal tides detected in FORMOSAT-3/COSMIC temperature data, *J. Geophys. Res.*, *115*, D14108, doi:10.1029/2009JD013008.
Remsberg, E. E., et al. (2008), Assessment of the quality of the Version 1.07 temperature-versus-pressure profiles of the middle atmosphere from TIMED/SABER, *J. Geophys. Res.*, *113*, D17101, doi:10.1029/2008JD010013.
Ricciardulli, L., and P. D. Sardeshmukh (2002), Local time and space changes of organized tropical deep convection, *J. Clim.*, *15*, 2775–2790.
Russell, J. M., III, M. G. Mlynczak, L. L. Gordley, J. Tansock, and R. Esplin (1999), An overview of the SABER experiment and preliminary calibration results, *Proc. SPIE Int. Soc. Opt. Eng.*, *3756*, 277–288.
Sakazaki, T., M. Fujiwara, X. Zhang, M. E. Hagan, and J. M. Forbes (2012), Diurnal tides from the troposphere to the lower mesosphere as deduced with TIMED/SABER satellite data and six global reanalysis data sets, *J. Geophys. Res.*, *117*, D13108, doi:10.1029/2011JD017117.
Sakazaki, T., et al. (2013), Diurnal ozone variations in the stratosphere revealed in observations from the Superconducting Submillimeter-Wave Limb-Emission Sounder (SMILES) on board the International Space Station (ISS), *J. Geophys. Res. Atmos.*, *118*, 2991–3006, doi:10.1002/jgrd.50220.
Sakazaki, T., M. Shiotani, M. Suzuki, D. Kinnison, J. M. Zawodny, M. McHugh, and K. A. Walker (2015), Sunset-sunrise difference in solar occultation ozone measurements (SAGE II, HALOE, and ACE-FTS) and its relationship to tidal vertical winds, *Atmos. Chem. Phys.*, *15*, 829–843.
Salby, M. L., H. H. Hendon, K. Woodberry, and K. Tanaka (1991), Analysis of global cloud imagery from multiple satellites, *Bull. Am. Meteorol. Soc.*, *72*, 467–480.
Sassi, F., and R. R. Garcia (1997), The role of equatorial waves forced by convection in the tropical semiannual oscillation, *J. Atmos. Sci.*, *54*, 1925–1942.
Sato K., S. Watanabe, Y. Kawatani, Y. Tomikawa, K. Miyazaki, and M. Takahashi (2009), On the origins of mesospheric gravity waves, *Geophys. Res. Lett.*, *36*, L19801, doi:10.1029/2009GL039908.
Sato, K., S. Tateno, S. Watanabe, and Y. Kawatani (2012), Gravity wave characteristics in the Southern Hemisphere revealed by a high-resolution middle-atmosphere general circulation model, *J. Atmos. Sci.*, *69*, 1378–1396, doi:10.1175/JAS-D-11-0101.1.
Scherllin-Pirscher, B., G. Kirchengast, A. K. Steiner, Y.-H. Kuo, and U. Foelsche (2011), Quantifying uncertainty in climatological fields from GPS radio occultation: An empirical-analytical error model, *Atmos. Meas. Tech.*, *4*, 2019–2034, doi:10.5194/amt-4-2019-2011.
SPARC, Assessment of Upper Tropospheric and Stratospheric Water Vapour (2000), SPARC Rep. No. 2.

Suvorova, E. V., and A. I. Pogoreltsev (2011), Modeling of nonmigrating tides in the middle atmosphere, *Geomagn. Aeron.*, *51*, 105–115.
Talaat, E. R., and R. S. Lieberman (1999), Nonmigrating diurnal tides in mesospheric and lower-thermospheric winds and temperatures, *J. Atmos. Sci.*, *56*, 4073–4087.
Teitelbaum, H., and F. Vial (1991), On tidal variability induced by nonlinear interaction with planetary waves, *J. Geophys. Res.*, *96*(A8), 14,169–14,178, doi:10.1029/91JA01019.
Tokioka, T., and I. Yagai (1987), Atmospheric tides appearing in a global atmospheric general circulation model, *J. Meteorol. Soc. Jpn.*, *65*, 423–437.
Tomikawa, T., K. Sato, S. Watanabe, Y. Kawatani, K. Miyazaki, and M. Takahashi (2008), Wintertime temperature maximum at the subtropical stratopause in a T213L256 GCM, *J. Geophys. Res.*, *113*, D17117, doi:10.1029/2008JD009786.
Tomikawa, Y., K. Sato, S. Watanabe, Y. Kawatani, K. Miyazaki, and M. Takahashi (2012), Growth of planetary waves and the formation of an elevated stratopause after a major stratospheric sudden warming in a T213L256 GCM, *J. Geophys. Res.*, *117*, D16101, doi:10.1029/2011JD017243.
Wallace, J. M., and R. F. Tadd (1974), Some further results concerning the vertical structure of atmospheric tidal motions within the lowest 30 kilometers, *Mon. Weather Rev.*, *102*, 795–803.
Watanabe, S., Y. Kawatani, Y. Tomikawa, K. Miyazaki, M. Takahashi, and K. Sato (2008), General aspects of a T213L256 middle atmosphere generation circulation model, *J. Geophys. Res.*, *113*, D12110, doi:10.1029/2008JD010026.
Watanabe, S., Y. Tomikawa, K. Sato, Y. Kawatani, K. Miyazaki, and M. Takahashi (2009), Simulation of the eastward 4-day wave in the Antarctic winter mesosphere using a gravity wave resolving general circulation model, *J. Geophys. Res.*, *114*, D16111, doi:10.1029/2008JD011636.
Williams, C. R., and S. K. Avery (1996), Diurnal nonmigrating tidal oscillations forced by deep convective clouds, *J. Geophys. Res.*, *101*(D2), 4079–4091, doi:10.1029/95JD03007.
Xie, F., D. L. Wu, C. O. Ao, and A. J. Mannucci (2010), Atmospheric diurnal variations observed with GPS radio occultation soundings, *Atmos. Chem. Phys.*, *10*, 6889–6899.
Xu, J., A. K. Smith, M. Liu, H. Gao, G. Jiang, and W. Yuan (2013), Evidence for nonmigrating tides produced by the interaction between tides and stationary planetary waves in the stratosphere and lower mesosphere, *J. Geophys. Res. Atmos.*, *119*, 471–489, doi:10.1002/2013JD020150.
Yoshikawa, M., and S. Miyahara (2005), Excitations of nonmigrating diurnal tides in the mesosphere and lower thermosphere simulated by the Kyushu-GCM, *Adv. Space Res.*, *35*, 1918–1924.
Zeng, Z., W. Randel, S. Sokolovskiy, C. Deser, Y.-H. Kuo, M. Hagan, J. Du, and W. Ward (2008), Detection of migrating diurnal tide in the tropical upper troposphere and lower stratosphere using the Challenging Minisatellite Payload radio occultation data, *J. Geophys. Res.*, *113*, D03102, doi:10.1029/2007JD008725.
Zhang, X., J. M. Forbes, M. E. Hagan, J. M. Russell III, S. E. Palo, C. J. Mertens, and M. G. Mlynczak (2006), Monthly tidal temperatures 20–120 km from TIMED/SABER, *J. Geophys. Res.*, *111*, A10S08, doi:10.1029/2005JA011504.
Zhang, X., J. M. Forbes, and M. E. Hagan (2010a), Longitudinal variation of tides in the MLT region: 1. Tides driven by tropospheric net radiative heating, *J. Geophys. Res.*, *115*, A06316, doi:10.1029/2009JA014897.
Zhang, X., J. M. Forbes, and M. E. Hagan (2010b), Longitudinal variation of tides in the MLT region: 2. Relative effects of solar radiative and latent heating, *J. Geophys. Res.*, *115*, A06317, doi:10.1029/2009JA014898.
Zhang, X., J. M. Forbes, and M. E. Hagan (2012), Seasonal-latitudinal variation of the eastward propagating diurnal tide with zonal wave number 3 in the MLT: Influences of heating and background wind distribution, *J. Atmos. Terr. Phys.*, *78–79*, 37–43, doi:10.1016/j.jastp.2011.03.005.